

# A fully organic retinal prosthesis restores vision in a rat model of degenerative blindness

José Fernando Maya-Vetencourt<sup>1†</sup>, Diego Ghezzi<sup>1†‡</sup>, Maria Rosa Antognazza<sup>2</sup>, Elisabetta Colombo<sup>1</sup>, Maurizio Mete<sup>3</sup>, Paul Feyen<sup>1</sup>, Andrea Desii<sup>2</sup>, Ambra Buschiazzo<sup>4</sup>, Mattia Di Paolo<sup>5</sup>, Stefano Di Marco<sup>5</sup>, Flavia Ticconi<sup>4</sup>, Laura Emionite<sup>6</sup>, Dmytro Shmal<sup>1</sup>, Cecilia Marini<sup>7</sup>, Ilaria Donelli<sup>8</sup>, Giuliano Freddi<sup>8</sup>, Rita Maccarone<sup>5</sup>, Silvia Bisti<sup>5</sup>, Gianmario Sambuceti<sup>4</sup>, Grazia Pertile<sup>3</sup>, Guglielmo Lanzani<sup>2</sup> and Fabio Benfenati<sup>1,9\*</sup>

**The degeneration of photoreceptors in the retina is one of the major causes of adult blindness in humans. Unfortunately, no effective clinical treatments exist for the majority of retinal degenerative disorders. Here we report on the fabrication and functional validation of a fully organic prosthesis for long-term *in vivo* subretinal implantation in the eye of Royal College of Surgeons rats, a widely recognized model of retinitis pigmentosa. Electrophysiological and behavioural analyses reveal a prosthesis-dependent recovery of light sensitivity and visual acuity that persists up to 6–10 months after surgery. The rescue of the visual function is accompanied by an increase in the basal metabolic activity of the primary visual cortex, as demonstrated by positron emission tomography imaging. Our results highlight the possibility of developing a new generation of fully organic, highly biocompatible and functionally autonomous photovoltaic prostheses for subretinal implants to treat degenerative blindness.**

The progressive degeneration of retinal photoreceptors due to single mutations in any of over 240 identified genes (RetNet, Retinal Information Network) is one of the major causes of adult blindness in humans<sup>1,2</sup>. Among these pathologies, retinitis pigmentosa, a collective name for a set of genetic disorders that cause death of photoreceptors, afflicts 1 person in every 4,000 worldwide<sup>3</sup> and has no effective clinical treatment thus far.

A variety of therapeutic approaches have been developed in animal models of retinal degenerative diseases<sup>4–8</sup>. Numerous research groups attempted to promote the reinstatement of vision by electrically stimulating residual neuronal circuitries in the degenerate retina using prosthetic implants in the epiretinal<sup>9,10</sup>, subretinal<sup>11–14</sup> or suprachoroidal<sup>15</sup> configuration. Encouraging results from clinical trials using these systems have been reported recently<sup>16–19</sup> (for reviews, see refs 20,21). However, most of the prostheses face various limitations that include the mechanical mismatch with soft retinal tissues, as well as the complexity of the manufacturing process and operational principles. Moreover, they often require trans-ocular cables to connect with an external wireless receiver and electrical stimulator, and/or an external image-capturing camera, which further limit the tolerability of the prosthetic approach.

Recently, an epiretinal prosthesis with an intraocular wireless receiver and stimulator was reported<sup>22</sup>. Despite powering only a limited number of electrodes, which restricts spatial resolution,

this approach avoids the necessity of using a trans-scleral cable. A second step overcoming the current limitations of retinal prostheses was achieved by the development of a new concept of photovoltaic stimulation<sup>12–14</sup>. In this configuration, infrared light entering the pupil is converted into electrical stimuli delivered to the retina without the need of implanted electronics or physical connection with external devices. The major issue of such an approach is however the low sensitivity that essentially hampers the application at daylight illumination.

In the framework of photovoltaic retinal prosthesis, we recently introduced organic conjugated polymers as interfaces for neuronal photostimulation<sup>23–26</sup>. The use of conjugated polymers to manufacture subretinal prostheses offers several advantages as compared with previously reported approaches, namely multiple photostimulation mechanisms, including photovoltaic functioning, high biocompatibility, mechanical compliance, and sensitivity close to daylight range. In this work, we developed a fully organic device composed of a flexible and highly conformable silk substrate covered with photoactive layers of conjugated polymers and implanted it in the subretinal space of dystrophic Royal College of Surgeons (RCS) rats, a widely recognized model of retinitis pigmentosa<sup>27</sup>. The analysis of its efficacy in the recovery of visual functions revealed a significant and persistent prosthesis-induced rescue of vision in RCS dystrophic rats that lasted up to 6–10 months after implantation and was associated with a full

<sup>1</sup>Center for Synaptic Neuroscience and Technology, Istituto Italiano di Tecnologia, 16132 Genoa, Italy. <sup>2</sup>Center for Nano Science and Technology, Istituto Italiano di Tecnologia, 20133 Milan, Italy. <sup>3</sup>Ophthalmology Department, Sacro Cuore Hospital—Don Calabria, 37024 Negrar, Italy. <sup>4</sup>Department of Health Science, Nuclear Medicine, University of Genoa, 16132 Genoa, Italy. <sup>5</sup>Department of Biotechnology and Applied Clinical Science, University of L'Aquila, 67100, Italy. <sup>6</sup>Animal Facility, National Institute Cancer Research, IRCCS AOU San Martino-IST, 16132 Genoa, Italy. <sup>7</sup>Institute of Molecular Bio-imaging and Physiology (IBFM), CNR, 16163 Milan (GE section), Italy. <sup>8</sup>Innovhub-SSI, Silk Division, 20133 Milan, Italy. <sup>9</sup>Department of Experimental Medicine, University of Genoa, 16132 Genoa, Italy. <sup>†</sup>These authors contributed equally to this work. <sup>‡</sup>Present address: Center for Neuroprosthetics, Interfaculty Institute of Bioengineering, School of Engineering, École Polytechnique Fédérale de Lausanne, 1015 Lausanne, Switzerland. \*e-mail: [fabio.benfenati@iit.it](mailto:fabio.benfenati@iit.it)

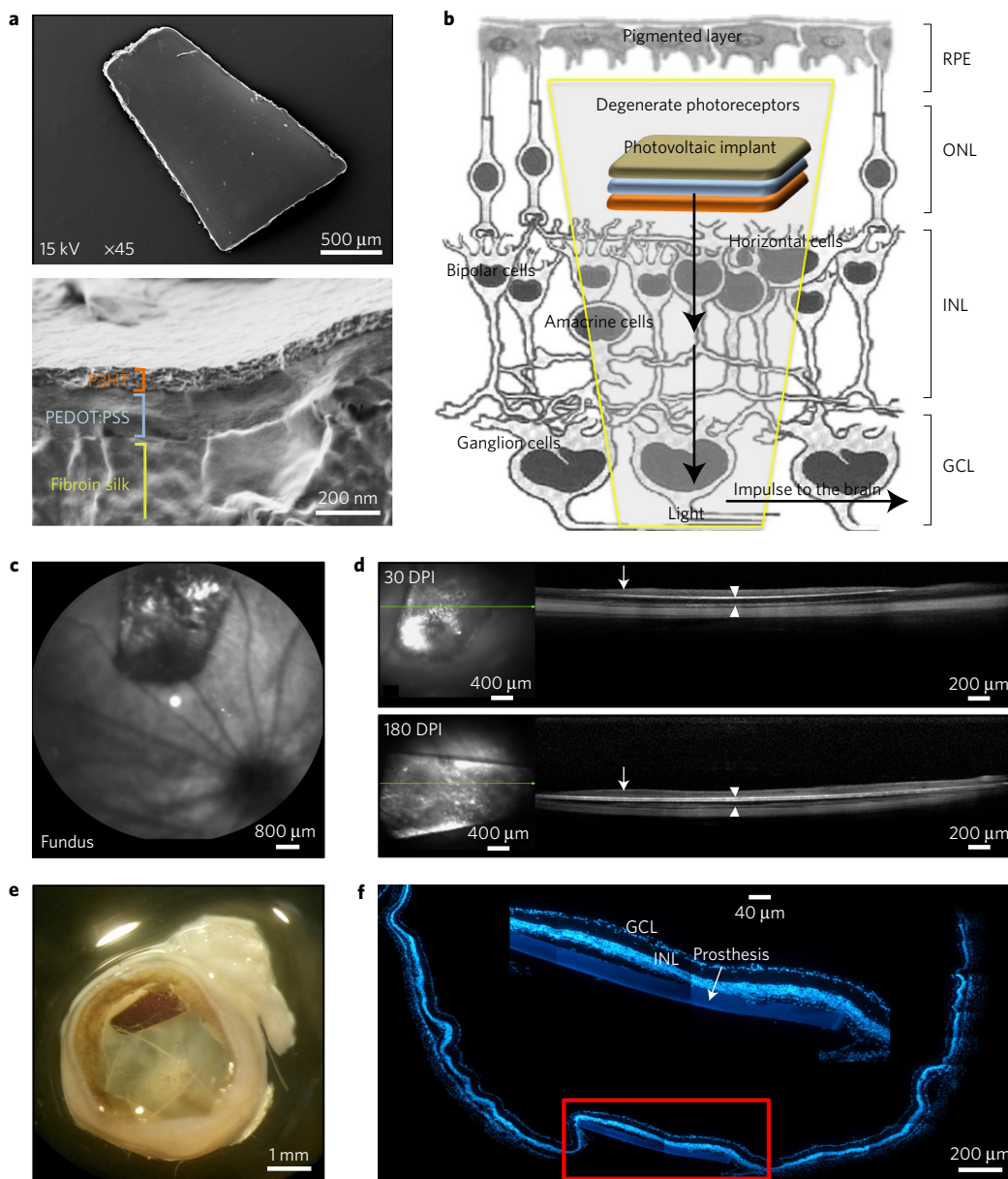


**Figure 1 | The organic prosthesis and the subretinal implant.** **a**, Scanning electron microscopy images of the full prosthetic device (top) and of its cross-section at higher magnification showing the three-layered structure (bottom). **b**, Scheme of the subretinal implant strategy. RPE, retinal pigment epithelium; ONL, outer nuclear layer; INL, inner nuclear layer; GCL, ganglion cell layer. **c**, Sample confocal scanning laser ophthalmoscopy image of the surgical prosthesis placement in the eye fundus of a dystrophic RCS rat. **d**, OCT analysis showing the strict contact between the retina (arrows) and the implant (arrowheads) at 30 and 180 dots per inch (DPI). No retinal detachments or breakages were observed. **e, f**, Explanted eye fixed (**e**), stained with bisbenzimidazole and acquired by confocal microscopy (**f**) to identify retinal nuclear layers and the position of the device. The high-magnification image (red box) shows the integrity and location of the implant in the retina.

structural and functional preservation of the opto-neural interface. These results highlight the potential clinical relevance of this fully organic prosthesis in retinal degenerative blindness.

### Subretinal implant of the organic prosthesis in RCS rats

We fabricated a fully organic multi-layered device composed of a superficial semiconductive layer of poly(3-hexylthiophene) (P3HT), an intermediate conductive layer of poly(3,4-ethylenedioxythiophene)-poly(styrenesulfonate) (PEDOT:PSS), and a silk fibroin layer (average thickness, 30 μm) as a passive substrate. The dimension, shape and multilayer structure of the prosthesis are shown in Fig. 1a (upper and lower panels). The PEDOT:PSS and P3HT layers were sequentially spin-coated on crystallized silk from

*Bombyx mori* cocoons (see Methods). The device was cut in shape and size suitable for implantation by a laser-assisted technique. To verify the specificity of the conjugated-polymer-based interface and rule out secondary effects on the retina due to the implant *per se*, we manufactured a silk-only device with the same procedure, geometry and dimensions of the full device, but lacking the thin polymeric films (average total thickness, 800 nm).

The prosthetic device was implanted in the subretinal space of 2–3-month-old dystrophic RCS rats, as previously described<sup>28,29</sup>. At this age, RCS rats already show marked impairments in both light sensitivity and spatial acuity, as assessed both electrophysiologically<sup>30</sup> and behaviourally<sup>31</sup>. The silk-PEDOT:PSS-P3HT prosthesis was implanted in the temporal hemi-retina of

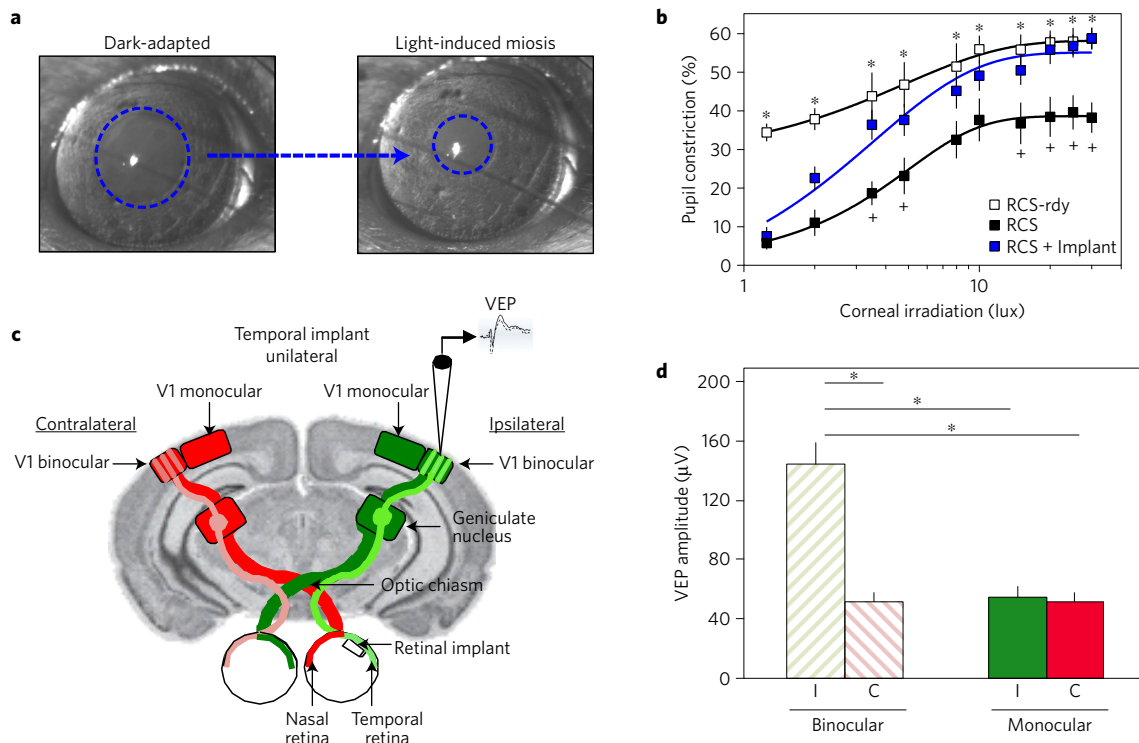


**Figure 2 | Pupillary reflex and topographic specificity of the prosthesis signal at the cortical level.** **a**, Constriction of the pupil by light pulses as assessed using standard infrared imaging in implanted RCS rats at 30 DPI. **b**, Quantification of the PLR as a function of light intensity, showing the prosthesis-induced recovery of light sensitivity in RCS rats at 30 DPI at intensities  $>2$  lux. Data are means  $\pm$  s.e.m. \* $p < 0.05$  versus RCS; + $p < 0.05$  versus RCS + Implant; two-way analysis of variance (ANOVA) for repeated measures, Tukey's multiple comparison test (RCS-*rdy* controls,  $n = 6$ ; non-implanted RCS rats,  $n = 11$ ; implanted RCS rats,  $n = 15$ ). **c**, Sketch of the temporal projections of the retina to the ipsilateral (light green) and contralateral (light red) areas of the binocular cortex and of the position of the unilateral implant in the RCS rat. **d**, The significant increase of the ipsilateral (binocular) cortical responses to visual stimuli highlights the spatial correlation between the implant location in the retina and the response in the corresponding cortical projection areas. I, C: ipsilateral and contralateral, respectively, for both binocular and monocular areas of the visual cortex. Cortical response amplitudes (means  $\pm$  s.e.m.) were: ipsilateral binocular,  $144.4 \pm 7.3 \mu\text{V}$ ; contralateral binocular,  $54.4 \pm 3.5 \mu\text{V}$ ; ipsilateral monocular,  $51.4 \pm 3.0 \mu\text{V}$ ; contralateral monocular,  $51.7 \pm 1.3 \mu\text{V}$  ( $n = 4$ ). One-way ANOVA/*post hoc* Tukey's multiple comparison test, \* $p < 0.0001$ .

anaesthetized animals, taking care to place it between the retinal pigment epithelium and the inner nuclear layer of the retina (Fig. 1b). Near-infrared retinographies obtained by confocal scanning laser ophthalmoscopy were used to localize the prosthetic device, evaluate the retinal coverage (approximately 10–15%) and determine its relationship with the inner retina at both 30 and 180 days post-implant (DPI). The distance between the implant and the optic nerve was used to verify the centrality of the device within the fundus (Fig. 1c). Analysis by means of optical coherence tomography (OCT) revealed that the retina remained well attached over the entire area of the implant during the follow-up period (Fig. 1d). Retinal integrity was seen above and around the implant and no swelling or delamination effects of the device were observed (Fig. 1e,f). This is in agreement with previous observations that the implant in normal rats elicited a modest and transient inflammatory reaction that decreased soon after surgery with full preservation of retinal morphology<sup>28,29</sup>.

### Rescue of the pupillary reflex

As an initial evaluation of the device performance, we used the pupillary light reflex (PLR). This subcortical response can be considered an index of light sensitivity, as it reflects the complementary function of the rod–cone system and the melanopsin-associated system<sup>32</sup>. We evaluated the PLR in bilaterally implanted, dark-adapted animals at 30 DPI using light stimuli of increasing intensity (1–30 lux). This response is largely reduced in degenerative retinal diseases. Indeed, the percentage

of pupil constriction (Fig. 2a) was largely impaired in dystrophic RCS rats with respect to non-dystrophic RCS-*rdy* controls at all irradiation intensities tested (Fig. 2b). In contrast, age-matched implanted dystrophic RCS rats at 30 DPI (Supplementary Movie 1) fully recovered the pupillary response to levels indistinguishable from non-dystrophic controls at irradiation intensities  $>2$  lux. This indicates that the prosthesis renders the retina of RCS dystrophic rats sensitive to light.

### Specificity of the prosthesis-generated cortical signals

We next focused our attention on the response to light at the cortical level. We assessed the specificity of the electrical signal driven by the implanted prosthesis in the primary visual cortex (V1) at 30 DPI by recording visual evoked potentials (VEPs) driven by flashes of light ( $20 \text{ cd m}^{-2}$ ; 100 ms). Particular care was taken in positioning the subretinal implant unilaterally in the temporal hemi-retina of RCS rats. Considering the anatomy of the rat retinal projections to V1 (ref. 33), it can be predicted that the prosthesis-generated electrical signals, after unilateral placement of the device in the temporal hemi-retina, are observed only in the binocular region of V1 (Oc1b) ipsilateral to the implant (Fig. 2c; light green). Accordingly, the amplitude of the cortical response measured in the ipsilateral Oc1b after binocular visual stimulation was nearly threefold higher than the amplitude recorded in the contralateral Oc1b (Fig. 2d). The former signal was also significantly larger than that observed in the monocular areas of the ipsilateral and contralateral cortex. As such, the observed light-driven electrical

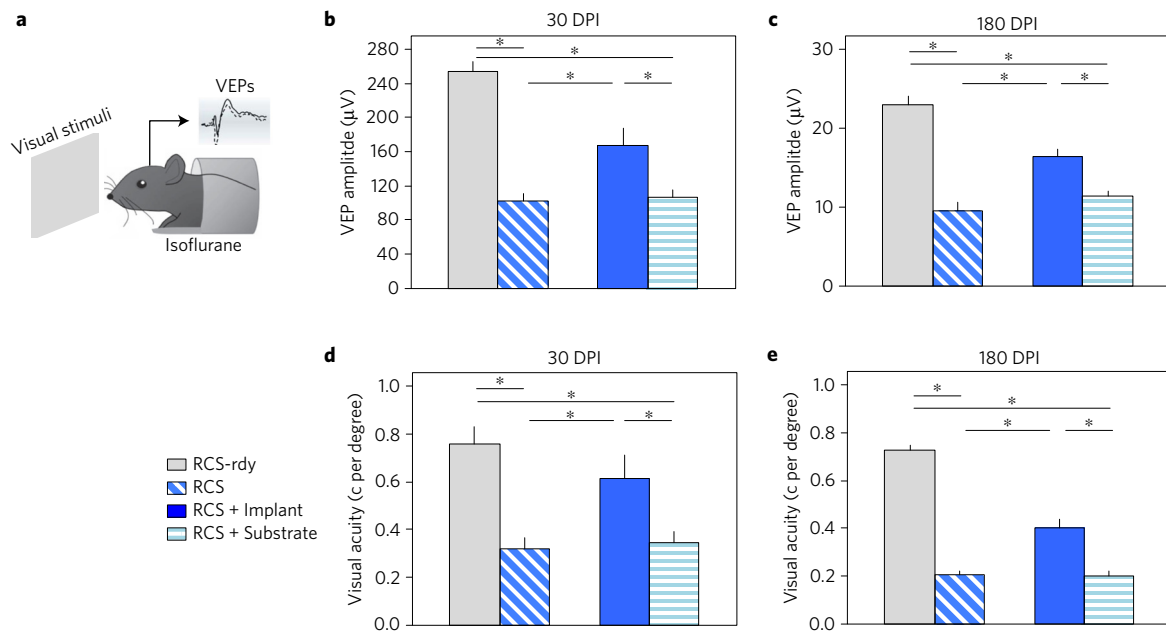


**Figure 3 | Electrophysiological assessment of cortical visual responses in response to flash and patterned illumination.** **a–c**, VEP recordings in V1 (**a**) in response to flash stimuli ( $20 \text{ cd m}^{-2}$ ; 100 ms) show the rescue of light sensitivity in implanted RCS rats at both 30 DPI (**b**) and 180 DPI (**c**). The mean ( $\pm$ s.e.m.) amplitudes of the V1 response at 30 DPI were: RCS-rdy,  $253.4 \pm 12.3 \mu\text{V}$  ( $n=8$ ); RCS,  $102.8 \pm 7.5 \mu\text{V}$  ( $n=8$ ); RCS + Implant,  $167.0 \pm 21.1 \mu\text{V}$  ( $n=7$ ); RCS + Substrate,  $107.2 \pm 8.2 \mu\text{V}$  ( $n=7$ ). The mean ( $\pm$ s.e.m.) amplitudes of the V1 response at 180 DPI were: RCS-rdy,  $23.0 \pm 1.05 \mu\text{V}$  ( $n=8$ ); RCS,  $9.54 \pm 1.05 \mu\text{V}$  ( $n=8$ ); RCS + Implant,  $16.38 \pm 1.02 \mu\text{V}$  ( $n=8$ ); RCS + Substrate,  $11.38 \pm 0.73 \mu\text{V}$  ( $n=8$ ). **d,e**, The electrophysiological analysis of VEP recordings in response to horizontal sinusoidal gratings of increasing spatial frequencies (0.1 to 1 cycle per degree of visual angle) administered at 0.5 Hz reveals a significant recovery of visual acuity at both 30 DPI (**d**) and 180 DPI (**e**). The mean ( $\pm$ s.e.m.) spatial acuity values at 30 DPI were: RCS-rdy,  $0.76 \pm 0.02$  cycles per degree ( $n=10$ ); RCS,  $0.32 \pm 0.01$  cycles per degree ( $n=10$ ); RCS + Implant,  $0.62 \pm 0.03$  cycles per degree ( $n=10$ ); RCS + Substrate,  $0.34 \pm 0.02$  cycles per degree ( $n=7$ ). The mean ( $\pm$ s.e.m.) spatial acuity values at 180 DPI were: RCS-rdy,  $0.73 \pm 0.02$  cycles per degree ( $n=8$ ); RCS,  $0.2 \pm 0.02$  cycles per degree ( $n=9$ ); RCS + Implant,  $0.38 \pm 0.02$  cycles per degree ( $n=12$ ); RCS + Substrate,  $0.19 \pm 0.02$  cycles per degree ( $n=8$ ). One-way ANOVA/*post hoc* Tukey's multiple comparison test: \* $0.0001 < p < 0.01$  (**b**); \* $0.0001 < p < 0.05$  (**c**); \* $p < 0.0001$  (**d,e**).

signal at the cortical level topographically corresponds to the light-dependent activation of the inner retina circuitry harbouring the prosthesis and is not attributable to a trophic effect of the implant and/or of its electrical activity on the adjacent retina, as previously reported<sup>11,34–36</sup>.

### Recovery of visual cortical responses

To quantitatively evaluate the extent of visual function restoration, we assessed light sensitivity in bilaterally implanted dystrophic RCS rats at 30 and 180 DPI using electrophysiological recordings of VEPs in Ocl1b of V1 (Fig. 3a). We measured the amplitude of the V1 response evoked by flash stimuli ( $20 \text{ cd m}^{-2}$ ; 100 ms) of low temporal frequency (0.5 Hz), as previously described<sup>37,38</sup>. A substantial recovery of light sensitivity was observed in implanted RCS rats at 30 DPI. As shown in Fig. 3b and Supplementary Fig. 1, the amplitude of the V1 response in non-implanted dystrophic RCS animals was nearly 2.5-fold lower as compared with non-dystrophic RCS-rdy controls. Notably, implanted age-matched dystrophic RCS rats showed a cortical response at 30 DPI that was higher in amplitude than that observed in either non-implanted (see above) or sham-implanted dystrophic RCS animals. A persistent rescue of light sensitivity (+71.6%) similar to the extent of the recovery at 30 DPI (+62.3%) was observed at 180 DPI in implanted RCS rats (Fig. 3c and Supplementary Fig. 2). The overall lower VEP amplitude observed in 9-month-old control and dystrophic RCS rats (the age corresponding to 180 DPI) is in agreement with the progressive photoreceptor loss that these pink-eyed RCS rats display over their lifespan, as previously reported<sup>39</sup>. Notably, a smaller cohort of animals examined at 300 DPI still revealed a significant twofold increase in the VEP amplitude in implanted RCS rats

with respect to either non-implanted or sham-implanted RCS rats (Supplementary Fig. 3).

Much like the reduction in the amplitude of the VEP signal, an increase in the time of VEP latency, can be ascribed to a functional alteration of the retinal circuitries<sup>40</sup>. In line with this, we observed a significant increase of the VEP latency in dystrophic RCS animals as compared with non-dystrophic RCS-rdy rats at both 30 and 180 DPI (Supplementary Fig. 4). This phenomenon matches the progression of photoreceptor degeneration and retinal rewiring causing the gradual decrease of vision in our experimental model. Interestingly, the longer VEP latency in dystrophic RCS animals was not rescued by the implant with respect to either non-implanted or sham-implanted RCS-rdy controls at both 30 and 180 DPI, further excluding the existence of a trophic effect of the implant on the adjacent retina.

We next shifted our attention to the spatial resolution. Measures of visual acuity were obtained by recording VEPs in Ocl1b of V1 (Fig. 3a) in response to patterned visual stimuli ( $20 \text{ cd m}^{-2}$ ; 0.5 Hz) of varying spatial frequency (0.1 to 1 cycle per degree), as previously described<sup>37,38</sup>. A significant recovery of spatial resolution was observed in implanted RCS rats at 30 DPI. As shown in Fig. 3d and Supplementary Fig. 5, spatial acuity in non-implanted RCS rats was markedly lower than that of non-dystrophic RCS-rdy controls. On the contrary, age-matched implanted RCS animals displayed a significant twofold enhancement of visual acuity at 30 DPI as compared with either non-implanted (see above) or sham-implanted RCS dystrophic animals. The rescue of visual acuity in implanted RCS rats at 180 DPI (+96.7%) was again closely similar to the effect observed at 30 DPI (+91.9%; Fig. 3e and Supplementary Fig. 6). Interestingly, a high correlation was

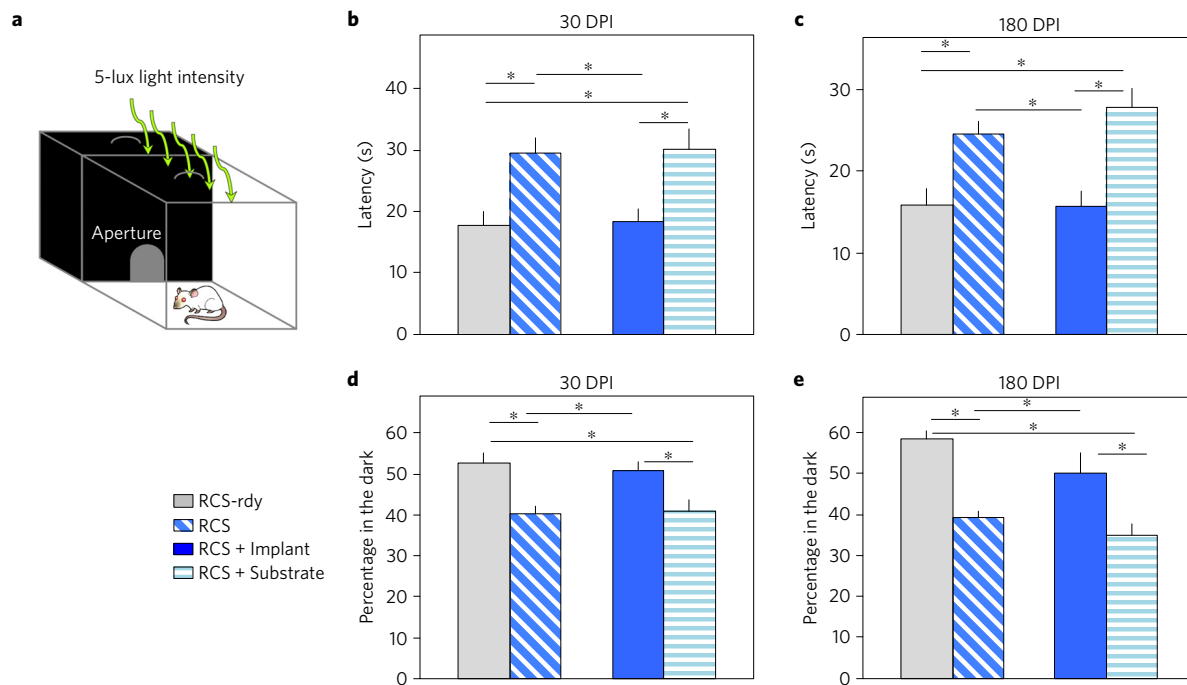


**Figure 4 | Behavioural evaluation of visual functions.** **a-c**, The light-dark box test (**a**) revealed the reinstatement of light sensitivity in implanted RCS rats evaluated as escape latency from the lit compartment at both 30 DPI (**b**) and 180 DPI (**c**). Mean ( $\pm$ s.e.m.) latencies at 30 DPI were: RCS-rdy,  $17.74 \pm 2.30$  s ( $n=46$ ); RCS,  $29.46 \pm 2.49$  s ( $n=41$ ); RCS + Implant,  $18.41 \pm 2.03$  s ( $n=44$ ); RCS + Substrate,  $30.07 \pm 3.29$  s ( $n=28$ ). Mean ( $\pm$ s.e.m.) latencies at 180 DPI were: RCS-rdy,  $15.86 \pm 2.04$  s ( $n=28$ ); RCS,  $24.50 \pm 1.57$  s ( $n=38$ ); RCS + Implant,  $15.71 \pm 1.86$  s ( $n=21$ ); RCS + Substrate,  $27.84 \pm 2.23$  s ( $n=19$ ). **d,e**, Implanted animals also showed a significant increase in the time spent in the dark compartment at both 30 DPI (**d**) and 180 DPI (**e**). Mean ( $\pm$ s.e.m.) percentages of time spent in the dark at 30 DPI: RCS-rdy,  $52.69 \pm 2.56\%$  ( $n=46$ ); RCS,  $40.37 \pm 1.76\%$  ( $n=41$ ); RCS + Implant,  $50.90 \pm 2.16\%$  ( $n=44$ ); RCS + Substrate,  $40.82 \pm 2.79\%$  ( $n=28$ ). Mean ( $\pm$ s.e.m.) percentages of time spent in the dark at 180 DPI: RCS-rdy,  $58.35 \pm 4.14$  s ( $n=28$ ); RCS,  $39.34 \pm 1.62$  s ( $n=38$ ); RCS + Implant,  $50.21 \pm 4.98$  s ( $n=21$ ); RCS + Substrate,  $34.93 \pm 2.85$  s ( $n=19$ ). One-way ANOVA/*post hoc* Tukey's multiple comparison test:  $*0.01 < p < 0.05$  (**b**);  $*0.001 < p < 0.01$  (**c**);  $*0.001 < p < 0.05$  (**d,e**).

found between gain in visual acuity and the goodness of prosthesis placement as determined by OCT analysis in a subgroup of the animals evaluated at 30 and 180 DPI (Supplementary Fig. 7;  $n=8$  per group).

### Recovery of visually driven behaviour

The next step was to assess vision in bilaterally implanted RCS rats at 30 and 180 DPI using the light-dark box test as a light-driven behavioural trial (Fig. 4a). This analysis relies on the innate aversion of nocturnal rodents to brightly illuminated areas<sup>41</sup>. Two parameters, namely the latency of escape from the illuminated area to darkness and the percentage of time spent in the dark using a 5-lux light intensity, were computed as an index of light sensitivity. As expected (Fig. 4b), non-implanted RCS animals displayed a longer latency than non-dystrophic RCS-rdy controls. In contrast, implanted dystrophic RCS animals at 30 DPI showed a significant recovery in the latency of escape as compared with either non-implanted or sham-implanted RCS rats, reaching levels indistinguishable from RCS-rdy controls (Supplementary Movie 2). The rescue in the escape latency in implanted RCS rats was fully preserved over time and still significant at 180 DPI (Fig. 4c and Supplementary Movie 3).

We also evaluated the time spent in the dark over the duration of the test. As shown in Fig. 4d, the percentage of time spent in the dark compartment by dystrophic RCS animals was significantly lower compared with non-dystrophic RCS-rdy controls. Conversely, implanted RCS rats at 30 DPI spent significantly more time in the dark than either non-implanted or sham-implanted RCS animals. The recovery of the time in the dark was fully preserved up to 180 DPI. No difference in the number of light-dark transitions was

detected at either 30 or 180 DPI (Supplementary Fig. 8), testifying that the experimental groups had a similar motor activity.

### Enhancement of basal metabolic activity in V1

We finally evaluated V1 metabolic activation in RCS rats at both 30 and 180 DPI by utilizing positron emission tomography (PET) neuroimaging after intravenous injection of the glucose analogue <sup>18</sup>F-fluoro-deoxyglucose (<sup>18</sup>F-FDG). This tracer enters neuronal cells according to their glucose consumption, is phosphorylated by hexokinase and accumulates within the cytosol being a false substrate for the enzymes directing glucose-6P to glycolysis<sup>42</sup>. Imaging of regional brain uptake thus provides a three-dimensional map of brain glucose consumption permitting us to estimate the metabolic activity of V1 (ref. 43) identified by a specific volume of interest (VOI). Average standardized uptake values (SUVs) were calculated to perform analysis of V1 activation, as previously described<sup>44</sup>. All experiments were performed in an environment with a light intensity of 5 lux. The <sup>18</sup>F-FDG uptake in V1 VOI in the four experimental groups at 30 and 180 DPI is shown in Fig. 5a,b. Dystrophic RCS animals at 30 DPI showed a significantly lower average SUV in V1 with respect to age-matched non-dystrophic RCS-rdy controls (Fig. 5c). Interestingly, the presence of the prosthesis was associated with a significant increase in average SUV as compared with those observed in either non-implanted (see above) or sham-implanted RCS animals. When analysed at 180 DPI, control and dystrophic RCS rats displayed an overall age-dependent decrease in SUV, consistent with the lower amplitude of VEP signals. However, the significant improvement in SUV was fully preserved over time in implanted dystrophic RCS rats and still significant at 180 DPI (Fig. 5d). Indeed, at this late time point, the average

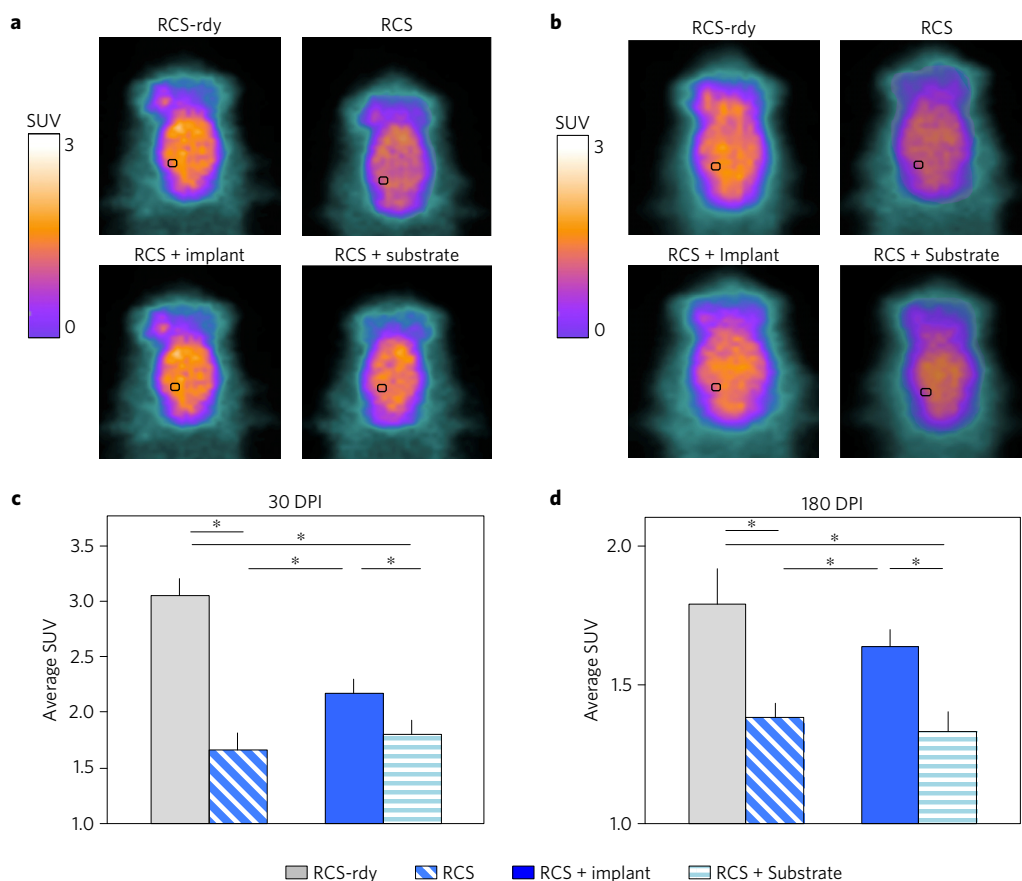


**Figure 5 | Basal metabolic activity in V1.** **a,b**, Representative images of basal metabolic activity acquired in all experimental groups at both 30 (**a**) and 180 DPI (**b**). The colour-scale map corresponding to the average SUV of  $^{18}\text{F}$ -FDG uptake over the scanned area is shown on the left. Inset black boxes show the location of the analysed average VOI in V1 ( $\sim 1\text{ mm}^3$ ). **c,d**, The quantitative analysis of the average SUV at 30 DPI (**c**) and 180 DPI (**d**) demonstrates a significant and persistent prosthesis-dependent increase in V1 basal metabolic activity. Mean ( $\pm$ s.e.m.) SUV values at 30 DPI were: RCS-rdy,  $3.05 \pm 0.156$  ( $n=7$ ); RCS,  $1.66 \pm 0.157$  ( $n=13$ ); RCS + Implant,  $2.17 \pm 0.125$  ( $n=16$ ); RCS + Substrate,  $1.81 \pm 0.130$  ( $n=8$ ). Mean ( $\pm$ s.e.m.) SUV values at 180 DPI were: RCS-rdy,  $1.792 \pm 0.127$  ( $n=7$ ); RCS,  $1.381 \pm 0.053$  ( $n=11$ ); RCS + Implant,  $1.624 \pm 0.046$  ( $n=14$ ); RCS + Substrate,  $1.330 \pm 0.07$  ( $n=8$ ). One-way ANOVA/*post hoc* Tukey's multiple comparison test:  $*0.0001 < p < 0.05$  (**c**);  $*0.01 < p < 0.05$  (**d**).

SUV in implanted RCS rats was still significantly higher than that measured in non-implanted or sham-implanted dystrophic RCS rats and virtually indistinguishable from the values observed in non-dystrophic RCS-rdy controls. These findings reveal a substantial and long-term rescue of basal metabolic activity in the visual cortex of dystrophic rats implanted with the retinal device.

### The rescue of vision is not due to a trophic effect

To unambiguously demonstrate that long-lasting rescue of visual functions was not attributable to a trophic effect of the implant and/or of the electrical activity on the adjacent retina, we performed histochemical studies in control and implanted retinæ 6 months after surgical implantation (Supplementary Figs 9–11). The analysis was carried out on retinal sections (from dorsal to ventral) that included the optic disc that were collected after 6 months from surgery or at the same age in control groups. Bisbenzimidazole nuclear labelling of retinal sections confirmed that, by the time of our analysis, all RCS animals, no matter whether they were not implanted, sham-implanted or implanted with the full device, completely lost almost all photoreceptors both in the implanted region and in the remaining retina, with no difference in the ratio between total and inner nuclear layer thicknesses (Supplementary Fig. 9). In addition, non-implanted RCS rats as well as RCS rats implanted with either the full device or the sham silk-only scaffold at 180 DPI showed similar expression levels of fibroblast growth factor

(FGF) mainly produced by Müller cells (Supplementary Fig. 10). Moreover, while both GFAP-positive astrocytes (Supplementary Fig. 10) and IBA1-positive microglial cells (Supplementary Fig. 11) were increased, as a result of the ongoing degeneration, in RCS retinæ with respect to non-dystrophic retinæ, the presence of the full device or of the silk-only scaffold did not significantly alter their proliferation with respect to age-matched non-implanted RCS rats.

### The device is preserved after long-term implantation

The long-lasting rescue of visual functions induced by the prosthesis indicates that the organic device is likely to be intact and active after months of implantation, despite the continuous exposure to biological fluids, body temperature and inflammatory cells. To demonstrate that, we performed structural, biophysical and electrophysiological analyses of post-mortem prostheses excised 6 months after implantation (Fig. 6). Analysis of the excised devices by light and fluorescence microscopy revealed that the prosthesis was intact and still covered by the fluorescent P3HT layer (Fig. 6a,b). Also, scanning electron microscopy (SEM) analysis of the prosthesis still embedded in the tissue revealed that the device was intact and in contact with the inner retina, with no apparent delamination (Fig. 6c,d). Analysis by SEM of the top and bottom surfaces of the device after dissection of the overlying retina revealed a completely different surface texture (Fig. 6e,f). The P3HT-covered surface was much smoother and uniform than the corresponding

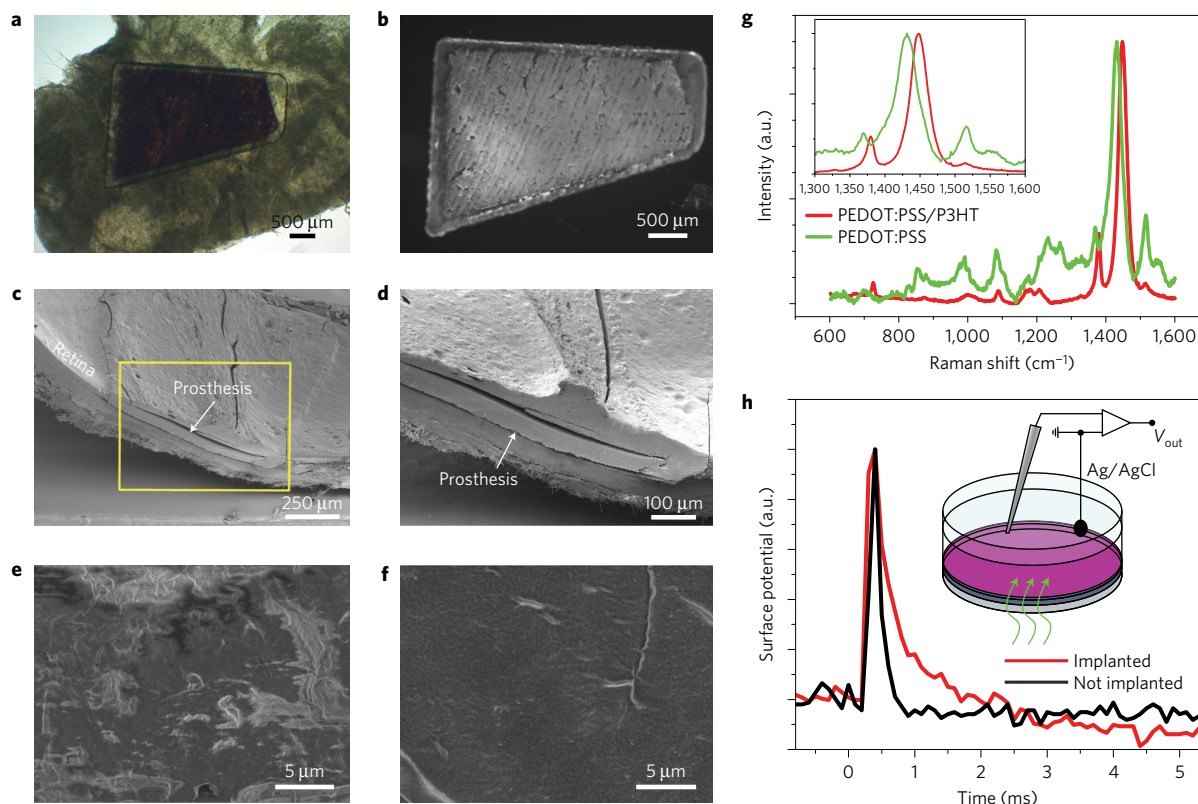


**Figure 6 | Characterization of the prosthesis after long-term implantation.** **a**, Optical image of a dissected retina with the prosthesis and its polymeric layer still in contact with the tissue. **b**, Fluorescence image (excitation: 540 nm; emission: 605 nm) of the same prosthesis after removal of the tissue showing the preserved photoluminescence of the P3HT layer after *in vivo* implantation. **c, d**, SEM image section view of a fixed retina where the prosthesis embedded in the tissue is clearly intact after 6 months of implantation; the magnified view of the area highlighted in yellow further confirms the complete confinement of the prosthesis in the subretinal space of the eye. **e, f**, Representative, top-view SEM images of the sham, silk-only (left) and full polymer (right) devices explanted from the rat retina 6 months after implantation and freed from the retinal tissues. The smooth surface of the full device testifies the persistence of the polymeric layer. **g**, Raman spectra of prosthetic implants, extracted from the subretinal space of RCS rats 6 months after implantation. The resonances in the range 1,350–1,500  $\text{cm}^{-1}$  (highlighted in the inset) demonstrate the presence and the preserved conjugation of the P3HT polymeric chains (red trace). The PEDOT:PSS signature in rare P3HT-free areas of the same device is also shown (green trace), confirming the absence of irreversible chemical degradation after implantation. **h**, Comparison between representative normalized surface potentials generated by implanted (red trace) and not-implanted (black trace) devices following green light stimulation (530 nm, 200  $\text{mW mm}^{-2}$ , 100 ms). Not-implanted devices were sterilized and aged for the same amount of time at room temperature in the dark. The fast light-evoked capacitive peak at the light onset ( $t = 0$  ms) is preserved 10 months after implantation. The not-implanted device was kept in the dark at room temperature for the same period of time. Inset: schematics of the experimental set-up used to record the surface potential with a micropipette electrode micromanipulated in the very close proximity of the P3HT/electrolyte interface.

silk-only sham implant, consistent with the low roughness of P3HT coating<sup>45</sup>. Next, Raman spectroscopy was used to test the irreversible chemical degradation of the polymer layers, typically breaking the conjugation along the chain bleaching the absorption (Fig. 6g). We focused on the 1,350–1,500  $\text{cm}^{-1}$  region, which corresponds to the carbon stretching modes. On excitation at 532 nm, two main peaks assigned to P3HT are observed at 1,448 and 1,380  $\text{cm}^{-1}$  (ref. 46). The PEDOT:PSS Raman modes at 1,431 and 1,369  $\text{cm}^{-1}$  are also visible, as expected<sup>47</sup>. Optoelectronic measurements completed the post-mortem analysis of the devices. A patch-clamp electrode positioned in close proximity of the P3HT/electrolyte interface was used to record the transient changes in the surface potential of the polymer layer evoked by illumination in devices explanted after 6 months *in vivo* or aged under ambient conditions in the dark (Fig. 6h). Notably, the explanted device still displayed a fast signal occurring in the first few milliseconds after photoexcitation, which has been previously attributed to the capacitive charging of the polymer/electrolyte interface<sup>25</sup>. These data demonstrate that both P3HT and PEDOT:PSS are still present and preserve their original properties after long-term implantation, with no evidence of any irreversible chemical degradation.

We report a fully organic, highly biocompatible, functionally autonomous, photosensitive prosthesis that rescues light sensitivity and spatial acuity in dystrophic RCS animals up to 10 months after implantation. The use of conjugated polymers, and more generally of organic materials, represents an innovation in the field of retinal prosthetic devices that might lead to a performance breakthrough. This experimental approach illustrates the possibility to work without implanted metal- or silicon-based electronics, thereby avoiding the need for power supply or external cameras. The prosthesis sensitivity corresponds to irradiances that fall within daylight illumination levels<sup>24</sup>, configuring a fully autonomous device, flexible to allow wide retina coverage, and with properties that are conserved over time in the presence of biological fluids. Moreover, the highly localized conjugated polymer response to light with a space constant of  $<50 \mu\text{m}$  (refs 23,24) produces a spatial resolution that is at least comparable to, if not higher than, that achieved by previous approaches using microelectrode or photodiode arrays of fixed, discrete geometries.

The restoration of visual functions induced by the prosthesis at distinct stages of disease progression in RCS rats suggests that this strategy may be of clinical relevance in both the early and

late phases of the pathology. The strong correlation between the recovery of visual acuity and the presence of the polymeric layers, and the substantially unaffected progression of retinal degeneration, demonstrate that the rescue of visual activity directly relies on the properties of the organic device and is not attributable to secondary trophic effects of the implant.

The results indicate that light-stimulated conjugated polymers directly activate residual neuronal circuitries in the degenerate retina. However, the detailed principle of operation of the prosthesis remains uncertain. We conjecture that it depends on the photo-generation of long-lived excited states, namely polarons, in the polymer layer and the subsequent interaction of such states with the retina environment. We recently demonstrated that illumination induces highly localized effects at the organic/electrolyte interface that include capacitive charging<sup>23,24</sup>, photo-thermal effects<sup>25,26</sup> and photo-electrochemical reactions<sup>48</sup>. The capacitive charging of the interface requires the presence of a conductive anode (PEDOT:PSS) to collect holes generated by photon absorption and accumulate negative charges at the polymer/water interface<sup>48</sup>. Light absorption by the polymer also leads to the generation of various photo-excited states that non-radiatively recombine to the ground state by locally releasing thermal energy. Both effects were demonstrated to modulate retinal activity in a time-dependent manner<sup>24,26</sup>, although the thermal effect is unlikely to be involved *in vivo*, since the energy levels involved, and the corresponding temperature increases, are much smaller as compared with *in vitro* experiments. The photoinduced accumulation of surface negative charge (p-type semiconducting behaviour) may lead to local ion redistribution, possibly causing a progressive acidification of the solution in the close proximity of the P3HT surface<sup>48</sup>. This could be an additional stimulus for the excitation of bipolar cells and/or retinal ganglion cells that express acid-sensing ion channels<sup>49</sup>.

Our results validate the use of organic semiconductors as functional materials in biocompatible and implantable devices. The study is the first *in vivo* and long-term application of an interface for neuronal photostimulation entirely made of organic conjugated polymers. This work demonstrates the far-reaching potential of the bioorganic approach in material science as recently discussed<sup>50</sup>. We use here an organic semiconductor that is typically used for photovoltaics. From photophysics to photobiology, the device exploits the transducing capability of the biotic/abiotic interface established by the polymer film with the retina inner cell layers. The significant rescue of visual functions that we found in an animal model of blindness due to photoreceptor degeneration makes it worth investigating the effects of this novel prosthesis in human patients afflicted by degenerative blindness.

## Methods

Methods, including statements of data availability and any associated accession codes and references, are available in the [online version of this paper](#).

Received 1 July 2016; accepted 31 January 2017;  
published online 6 March 2017

## References

- Wright, A. F., Chakarova, C. F., Abd El-Aziz, M. M. & Bhattacharya, S. S. Photoreceptor degeneration: genetic and mechanistic dissection of a complex trait. *Nat. Rev. Genet.* **11**, 273–284 (2010).
- Smith, A. J., Bainbridge, J. W. & Ali, R. R. Gene supplementation therapy for recessive forms of inherited retinal dystrophies. *Gene Ther.* **19**, 154–161 (2012).
- Hartong, D. T., Berson, E. L. & Dryja, T. P. Retinitis pigmentosa. *Lancet* **368**, 1795–1809 (2006).
- Frasson, M. *et al.* Retinitis pigmentosa: rod photoreceptor rescue by a calcium-channel blocker in the rd mouse. *Nat. Med.* **5**, 1183–1187 (1999).
- Leveillard, T. & Sahel, J. A. Rod-derived cone viability factor for treating blinding diseases: from clinic to redox signaling. *Sci. Transl. Med.* **2**, 26ps16 (2010).
- Busskamp, V. *et al.* Genetic reactivation of cone photoreceptors restores visual responses in retinitis pigmentosa. *Science* **329**, 413–417 (2010).
- Pearson, R. A. *et al.* Restoration of vision after transplantation of photoreceptors. *Nature* **485**, 99–103 (2012).
- Barber, A. C. *et al.* Repair of the degenerate retina by photoreceptor transplantation. *Proc. Natl Acad. Sci. USA* **110**, 354–359 (2013).
- Gerding, H., Benner, F. P. & Taneri, S. Experimental implantation of epiretinal retina implants (EPI-RET) with an IOL-type receiver unit. *J. Neural Eng.* **4**, S38–S49 (2007).
- Walter, P. *et al.* Cortical activation via an implanted wireless retinal prosthesis. *Invest. Ophthalmol. Vis. Sci.* **46**, 1780–1785 (2005).
- DeMarco, P. J. Jr *et al.* Stimulation via a subretinally placed prosthesis elicits central activity and induces a trophic effect on visual responses. *Invest. Ophthalmol. Vis. Sci.* **48**, 916–926 (2007).
- Mathieson, K. *et al.* Photovoltaic retinal prosthesis with high pixel density. *Nat. Photon.* **6**, 391–397 (2012).
- Mandel, Y. *et al.* Cortical responses elicited by photovoltaic subretinal prostheses exhibit similarities to visually evoked potentials. *Nat. Commun.* **4**, 1980 (2013).
- Lorach, H. *et al.* Photovoltaic restoration of sight with high visual acuity. *Nat. Med.* **21**, 476–482 (2015).
- Ayton, L. N. *et al.* First-in-human trial of a novel suprachoroidal retinal prosthesis. *PLoS ONE* **9**, e115239 (2014).
- Yanai, D. *et al.* Visual performance using a retinal prosthesis in three subjects with retinitis pigmentosa. *Am. J. Ophthalmol.* **143**, 820–827 (2007).
- Humayun, M. S. *et al.* Interim results from the international trial of Second Sight's visual prosthesis. *Ophthalmology* **119**, 779–788 (2012).
- Zrenner, E. *et al.* Subretinal electronic chips allow blind patients to read letters and combine them to words. *Proc. Biol. Sci.* **278**, 1489–1497 (2011).
- Stingl, K. *et al.* Artificial vision with wirelessly powered subretinal electronic implant alpha-IMS. *Proc. Biol. Sci.* **280**, 20130077 (2013).
- Zrenner, E. Will retinal implants restore vision? *Science* **295**, 1022–1025 (2002).
- Weiland, J. D., Cho, A. K. & Humayun, M. S. Retinal prostheses: current clinical results and future needs. *Ophthalmology* **118**, 2227–2237 (2011).
- Laube, T. *et al.* Development of surgical techniques for implantation of a wireless intraocular epiretinal retina implant in Gottingen minipigs. *Graefes. Arch. Clin. Exp. Ophthalmol.* **250**, 51–59 (2012).
- Ghezzi, D. *et al.* A hybrid bioorganic interface for neuronal photoactivation. *Nat. Commun.* **2**, 166 (2011).
- Ghezzi, D. *et al.* A polymer optoelectronic interface restores light sensitivity in blind rat retinas. *Nat. Photon.* **7**, 400–406 (2013).
- Martino, N. *et al.* Photothermal cellular stimulation in functional bio-polymer interfaces. *Sci. Rep.* **5**, 8911 (2015).
- Feyen, P. *et al.* Light-evoked hyperpolarization and silencing of neurons by conjugated polymers. *Sci. Rep.* **6**, 22718 (2016).
- Gal, A. *et al.* Mutations in MERTK, the human orthologue of the RCS rat retinal dystrophy gene, cause retinitis pigmentosa. *Nat. Genet.* **26**, 270–271 (2000).
- Di Paolo, M. *et al.* Inflammatory and morphological characterization of a foreign body retinal response. *Eur. J. Neurodegener. Dis.* **4**, 23–28 (2015).
- Antognazza, M. R. *et al.* Characterization of a polymer-based fully organic prosthesis for implantation into the subretinal space of the rat. *Adv. Healthc. Mater.* **5**, 2271–2282 (2016).
- Gias, C. *et al.* Degeneration of cortical function in the Royal College of Surgeons rat. *Vision Res.* **51**, 2176–2185 (2011).
- McGill, T. J., Douglas, R. M., Lund, R. D. & Prusky, G. T. Quantification of spatial vision in the Royal College of Surgeons rat. *Invest. Ophthalmol. Vis. Sci.* **45**, 932–936 (2004).
- Lucas, R. J. *et al.* Diminished pupillary light reflex at high irradiances in melanopsin-knockout mice. *Science* **299**, 245–247 (2003).
- Hubener, M. Mouse visual cortex. *Curr. Opin. Neurobiol.* **13**, 413–420 (2003).
- Morimoto, T. *et al.* Transcorneal electrical stimulation promotes the survival of photoreceptors and preserves retinal function in royal college of surgeons rats. *Invest. Ophthalmol. Vis. Sci.* **48**, 4725–4732 (2007).
- Ni, Y. Q., Gan, D. K., Xu, H. D., Xu, G. Z. & Da, C. D. Neuroprotective effect of transcorneal electrical stimulation on light-induced photoreceptor degeneration. *Exp. Neurol.* **219**, 439–452 (2009).
- Zhou, W. T. *et al.* Electrical stimulation ameliorates light-induced photoreceptor degeneration *in vitro* via suppressing the proinflammatory effect of microglia and enhancing the neurotrophic potential of Müller cells. *Exp. Neurol.* **238**, 192–208 (2012).
- Maya-Vetencourt, J. F. *et al.* The antidepressant fluoxetine restores plasticity in the adult visual cortex. *Science* **320**, 385–388 (2008).

38. Maya-Vetencourt, J. F. Experience-dependent expression of NPAS4 regulates plasticity in adult visual cortex. *J. Physiol.* **590**, 4777–4787 (2012).
39. LaVail, M. M. & Battelle, B. A. Influence of eye pigmentation and light deprivation on inherited retinal dystrophy in the rat. *Exp. Eye Res.* **21**, 167–192 (1975).
40. Lennerstrand, G. Delayed visual evoked cortical potentials in retinal disease. *Acta Ophthalmol. (Copenh)* **60**, 497–504 (1982).
41. Bourin, M. & Hascoet, M. The mouse light/dark box test. *Eur. J. Pharmacol.* **463**, 55–65 (2003).
42. Phelps, M. E. Positron computed tomography studies of cerebral glucose metabolism in man: theory and application in nuclear medicine. *Semin. Nucl. Med.* **11**, 32–49 (1981).
43. Paxinos, G. & Watson, C. *The Rat Brain in Stereotaxic Coordinates* Vol. 6 (Elsevier, 2007).
44. Hustinx, R., Smith, R. J., Benard, F., Bhatnagar, A. & Alavi, A. Can the standardized uptake value characterize primary brain tumors on FDG-PET? *Eur. J. Nucl. Med.* **26**, 1501–1509 (1999).
45. Vaquero Morata, S. *et al.* Organic semiconducting polymers for *in vitro* cell growth and photostimulation. *J. Mater. Chem. B* **4**, 5272–5283 (2016).
46. Tsoi, W. C. *et al.* The nature of in-plane skeleton Raman modes of P3HT and their correlation to the degree of molecular order in P3HT:PCBM blend thin films. *J. Am. Chem. Soc.* **133**, 9834–9843 (2011).
47. Stavvytska-Barba, M. & Myers Kelley, A. Surface-enhanced Raman study of the interaction of PEDOT:PSS with plasmonically active nanoparticles. *J. Phys. Chem. C* **114**, 6822–6830 (2010).
48. Mosconi, E. *et al.* Surface polarization drives photo-induced charge separation at the P3HT/water interface. *ACS Energy Lett.* **1**, 454–463 (2016).
49. Ettaiche, M., Deval, E., Cougnon, M., Lazdunski, M. & Voilley, N. Silencing acid-sensing ion channel 1a alters cone-mediated retinal function. *J. Neurosci.* **26**, 5800–5809 (2006).
50. Lanzani, G. Materials for bioelectronics: organic electronics meets biology. *Nat. Mater.* **13**, 775–776 (2014).

## Acknowledgements

The authors thank M. M. La Vail (Beckman Vision Center, University of California San Francisco, California) for providing non-dystrophic RCS-*rdy+* and dystrophic RCS rats; G. Vjifvinkel (Oftavinci BV, Geervliet, The Netherlands) for manufacturing specific surgical tools for implantation; L. Criante and S. Perissinotto for help at the laser micro-machining facility; M. Bramini and F. D. Fonzo for help in scanning electron microscopy; A. Russo, C. Orsini, F. Canu, I. Dall'Orto, A. Mehilli and D. Moruzzo for technical assistance. The work was supported by the EU project FP7-PEOPLE-212-ITN 316832 'OLIMPIA' (to F.B. and G.L.); Telethon—Italy (grants GGP12033 to G.L., F.B. and S.B. and GGP14022 to G.P. and F.B.); Fondazione Cariplo (project ONIRIS 2013–0738 to MRA, G.F. and D.G.); Compagnia di San Paolo (project ID 4191 to D.G. and F.B.), the Italian Ministry of Health (project RF-2013-02358313 to G.P., G.L. and F.B.) and Istituto Italiano di Tecnologia (pre-startup project to G.L. and F.B.). The support of Ra.Mo. Foundation (Milano, Italy) and Rare Partners srl (Milano, Italy) is also acknowledged.

## Author contributions

J.F.M.-V. and D.G. contributed equally to this work. J.F.M.-V. carried out *in vivo* electrophysiology experiments, behavioural analysis, and assisted in the PET trials; D.G. executed behavioural experiments, the PLR analysis, and preliminary electrophysiology; M.R.A. and A.D. fabricated and characterized the implants under the supervision of G.L.; I.D. and G.F. purified the silk protein used for the implants; M.M. and G.P. performed OCT analysis, developed and executed the surgical subretinal implantation; P.F. and E.C. carried out behavioural experiments; E.C. carried out the post-mortem studies on the devices; A.B., F.T., L.E., D.S. and C.M. executed PET experiments under the supervision of G.S.; M.D.P., S.D.M. and R.M. performed histological analysis under the supervision of S.B.; F.B. and G.L., conceived, supervised, and financed the project. J.F.M.-V., G.L. and F.B. wrote the manuscript. All authors discussed the experimental results and commented on the manuscript.

## Additional information

Supplementary information is available in the [online version of the paper](#). Reprints and permissions information is available online at [www.nature.com/reprints](http://www.nature.com/reprints). Correspondence and requests for materials should be addressed to F.B.

## Competing financial interests

The authors declare no competing financial interests.

## Methods

**Ethical approval and animal handling.** All animal manipulations and procedures were performed in accordance with the guidelines established by the European Community Council (Directive 2012/63/EU of 22 September 2010) and were approved by the Italian Ministry of Health (Authorization no. 645/2015-PR). Royal College of Surgeons inbred, pink-eyed dystrophic (RCS/LAV) animals, together with congenic non-dystrophic (RCS-rdy+/LAV) controls, were provided by M. M. La Vail (Beckman Vision Center, University of California San Francisco, California)<sup>39</sup>. Rat colonies were bred under standard conditions with *ad libitum* access to food and water under a 12:12 h light/dark cycle.

**Preparation of silk substrates.** Silk fibroin (SF) films were obtained from *Bombyx mori* cocoons. Cocoons were cut into two parts and immersed in distilled water, then treated at 120 °C for 30 min, and finally rinsed six times with distilled water, previously heated at 60 °C to remove sericin from fibres (degumming). The degummed fibres were stored for 3 days in a drying room, at 20 ± 2 °C and relative humidity of 65 ± 2%. They were then dissolved in a saturated lithium bromide (LiBr) solution inside a hermetically closed flask, and treated at 60 ± 2 °C for 3 h. The solution was then dissolved in distilled water, pre-heated at 60 °C and filtered. Dialysis was carried out to completely remove LiBr: the solution was poured into preconditioned cellulose tubes immersed in distilled water and continuously mechanically agitated. The solution was changed every 8 h for 3 days. Finally, the purified SF was filtered and drop-casted on Teflon Petri dishes. After 2 days, SF films (200 cm<sup>2</sup> area and 30 µm approximate thickness) were ready for the subsequent preparation steps.

**Microfabrication of the organic retinal prosthesis.** Prior to deposition of organic layers, SF thin films were sequentially rinsed in an ultrasonic bath with pure acetone and isopropanol for 7 min each. The temperature of the bath was carefully monitored and kept under 37 °C. After each rinse, substrates were gently dried using a nitrogen gun. Organic layers were deposited on the side in contact with the Teflon Petri dish during SF casting. PEDOT:PSS was used without further purification. A water dispersion was prepared by adding the following additives: the co-solvent dimethylsulfoxide (DMSO, 9% v/v) to increase the overall electrical conductivity; the crosslinker 3-glycidoxypropyltrimethoxysilane (GOPS, 0.9% v/v) to enhance the adhesion of the PEDOT:PSS layer to the substrate and avoid delamination; the surfactant Zonyl FS-300 (0.18% v/v) to promote dispersion wettability and facilitate the spin-coating process. In particular, GOPS, by acting as a crosslinking and adhesion agent, rendered PEDOT:PSS virtually water-insoluble, as shown by the fact that the volume increase during swelling passes from 155% to 35% (ref. 51). PEDOT:PSS dispersion including additives was then sonicated in an ultrasonic bath for 20 min and cooled at room temperature. PEDOT:PSS dispersion was deposited by spin-coating in two identical steps, by properly adjusting the rotation parameters (rotation speed 2,000 r.p.m., duration 60 s). The double deposition was required to limit the dynamic interaction between the PEDOT:PSS dispersion and the underlying SF film (that could lead to structural modifications and permeation of the substrate by the solvent), and to yield a uniform layer. Between the first and the second deposition, and after the second deposition, the substrates underwent a thermal annealing process in air (120 °C, 10 min). Poly-3-hexylthiophene (P3HT, 15,000–45,000 molecular weight) was used without further purification. The P3HT solution in chlorobenzene (30 g l<sup>-1</sup>) was sonicated for more than 1 h and deposited on top of the PEDOT:PSS layer by a two-step spin-coating process (800 r.p.m., 5 s; 1,600 r.p.m., 120 s). A final thermal annealing in a glove box (120 °C, 20 min) completed the fabrication of large-area devices (approximately 2 × 2 cm). From the large multilayer foil, retinal implants of dimensions suitable for implantation in rats were obtained through the step of laser-assisted cutting. The laser source was a regeneratively amplified diode-pumped mode-locked Yb:KGW laser with emission at 1,030 nm, repetition rate of 500 kHz and pulse width of 240 fs. The second harmonic beam, generated by a HIRO harmonics generator, was focused onto the polymer-coated SF substrates, with incidence from the substrate side. Pulse energy, in the order of 200 nJ, was adjusted to get a relatively sharp cut of the edges, without causing degradation to the optoelectronic properties of the active material. Samples were mounted on a three-axis motorized translation stage, and translation speed was set to 0.4 mm s<sup>-1</sup>. The cut was repeated three times to ensure an easy detachment of the sample from the support glass. The prosthesis has a trapezoid geometry, with dimensions suited to implantation in the rat subretinal space, namely 1.8 mm height, 1.1 mm and 0.55 mm parallel sides. Edges were intentionally smoothed during the laser-assisted fabrication to limit mechanical damage to retinal layers during surgery.

Sham SF-only devices were treated exactly as devices coated with conjugated polymers (P3HT and PEDOT:PSS). They were obtained from SF substrates fabricated and treated by using the very same protocol. Sham devices underwent the thermal treatments used in the PEDOT:PSS and P3HT annealing protocols, and were cut using the same laser procedure, obtaining trapezoidal shapes 1.8 mm in height and 1.1 mm and 0.55 mm parallel sides. After fabrication and prior to implantation, all samples were subjected to ethylene oxide sterilization.

**Surgical procedures.** Two/three-month-old RCS rats of either sex were anaesthetized with an intraperitoneal injection of diazepam (10 mg kg<sup>-1</sup>) followed by intramuscular administration of xylazine (5 mg kg<sup>-1</sup>) and ketamine (33 mg kg<sup>-1</sup>). The subretinal implant of the prosthesis was carried out as indicated below. Briefly, a 1.5 mm peritomy was made 2 mm posterior to the limbus, followed by a limbus-parallel incision through the sclera and choroid of approximately 1 mm. The retina was then gently detached from the choroid using a custom-designed spatula. Viscoelastic material was injected into the subretinal space and the device was inserted with the polymeric coating facing the retina. The edges of the sclerotomy were electrocoagulated and the conjunctiva apposed. Surgical procedures were carried out in a sterile room using a Leica ophthalmic surgical microscope. During the whole procedure, the rat eyes were kept wet. At the end of the surgical intervention, the position of the device was evaluated by indirect ophthalmoscopy. Topical application of antibiotic and cortisone to the eyes was performed to prevent inflammation of infection after the surgical procedure.

**In vivo imaging of the retinal implant.** Rats were anaesthetized with isoflurane (3% induction; 2% maintenance in oxygen) and their pupils dilated with 1% tropicamide eye drops before image acquisition. Confocal scanning laser ophthalmoscopy was performed with a commercially available scanning laser ophthalmoscope. Optical coherence tomography (OCT) was performed using the Spectralis HRA/OCT device. Each two-dimensional B-Scan recorded at 30° field of view consisted of 1,536 A-Scans acquired at a speed of 40,000 scans s<sup>-1</sup>. Imaging was performed using the proprietary software package Eye Explorer (version 3.2.1.0). The combination of laser scanning retinal imaging and OCT allowed a real-time tracking of eye movements and real-time averaging of OCT scans, thus reducing speckle noise in the OCT images considerably.

**Pupillary reflex.** Direct pupillary light reflex was assayed at 30 DPI or in age-matched RCS and RCS-rdy animals. Following dark-adaptation for at least 1 h, awake rats were manually held with the eye to be recorded perpendicular to an infrared-sensitive camera fitted with a Leica macro lens. Animals were subjected to a 2 s dim green light exposure of ascending irradiance provided by an LED source (515 nm) through the same macro lens. Sequential images were captured with a Hamamatsu camera at a 5 Hz frame rate. Background illumination was provided by an infrared LED source (850 nm) throughout the experiment. At least 10 min elapsed between exposures, during which time the animal was unrestrained in the dark. Subsequently, pupil area was determined from individual video frames before and after light exposure. To facilitate comparisons, pupil areas ( $a_t$ ) were expressed relative to the dilated area immediately prior to each exposure ( $a_0$ ). The effective intensity of each exposure was measured with a lux meter.

**In vivo electrophysiology.** Animals implanted with the prosthesis at either 30 or 180 DPI were anaesthetized with isoflurane (3% induction; 2% maintenance in oxygen) and placed in a stereotaxic frame. Anaesthesia level was stable throughout the experiment and body temperature was continuously monitored and maintained at ~37 °C by a thermostatic electric blanket. An ECG (electrocardiogram) was continuously monitored. A hole was drilled in the skull, corresponding to the binocular portion of the primary visual cortex (Oc1B). After exposure of the brain surface, the dura mater was gently removed, and a micropipette (2 MΩ) filled with NaCl (3 M) was inserted into the cortex 5 mm from  $\lambda$  (intersection between the sagittal and the lambdoid sutures). Both eyes were fixed, kept wet, and open throughout the analysis by means of adjustable metal rings surrounding the external portion of the eye bulb. We measured both light sensitivity and visual acuity using visual evoked potentials (VEPs), as described before<sup>37,38,52</sup>. During recording through one eye, the other was covered by a black adhesive tape. To prevent sampling bias, VEPs were recorded at three distinct penetrations within Oc1b, at 100 µm and 400 µm depths for each penetration. Signals were band-pass-filtered (0.1–100 Hz), amplified and fed to a computer for analysis, as described previously<sup>53</sup>. In the case of light sensitivity, visual stimuli were flashes of light (20 cd m<sup>-2</sup>; 100 ms), whereas in the case of spatial acuity, visual stimuli were horizontal sinusoidal gratings of increasing spatial frequencies (0.1 to 1 cycle per degree of visual angle) at 0.5 Hz. All visual stimuli were generated by a VSG2/2 card running custom software, presented on a monitor (20 × 22 cm area; 100% of contrast) positioned 20 cm from the rat's eyes, and centred on the previously determined receptive fields. Light sensitivity corresponded to the amplitude of the VEP response to flashes of light. Visual acuity was obtained by extrapolation to zero amplitude of the linear regression through the last four to five data points of VEP amplitude versus the log spatial frequency.

**Light-dark box test.** The light-dark test is a light-driven behavioural analysis based on the innate aversion of nocturnal rodents to brightly illuminated areas<sup>41</sup>. The test was used as an index of light sensitivity in all experimental groups at either 30 or 180 DPI. The trials were performed in a two-compartment box consisting of a 'light' compartment and a 'dark' compartment communicating through a small door (Fig. 4A) and positioned in an experimental room kept under dark

conditions. Animals were dark-adapted for 30 min. Soon (30 s) after introducing the animal in the 'light' compartment, illumination with a 5-lux intensity was switched on. Six-minute-video recordings were performed to monitor the latency of escape from the illuminated area and the percentage of time spent in each compartment. The number of transitions between the two compartments was also monitored and used as an index of light-independent motor activity.

**Positron emission tomography (PET) imaging.** Rats were kept under fasting conditions with free access to water for 6 h under the same artificial light. Rats were weighed and anaesthesia was induced by intraperitoneal administration of diazepam (4 mg kg<sup>-1</sup>) followed by intramuscular administration of ketamine/xylazine (5 mg kg<sup>-1</sup> and 33 mg kg<sup>-1</sup>, respectively). Serum glucose level was tested soon before the injection of 37–74 MBq <sup>18</sup>F-FDG through the tail vein. Animals were maintained under the same light conditions (5 lux) for 40 min and then positioned on the bed of a dedicated micro-PET system to undergo a scan acquisition of 600 s. PET data were reconstructed using a maximal likelihood expectation maximization method. An experienced observer in double blind conditions identified a volume of interest in the primary visual cortex (V1; ~1 mm<sup>3</sup>) using stereotaxic coordinates<sup>43</sup>, to measure the average standardized uptake value. This value represents the most commonly accepted index of <sup>18</sup>F-FDG retention and represents tracer uptake as the fraction of injected tracer dose normalized for body weight<sup>34</sup>.

**Histology and immunohistochemistry of the retina.** The study was carried out on retinal sections (from dorsal to ventral) that included the optic disc and that were collected after 6 months from surgery or at same age in control groups. Experimental animals were euthanized with CO<sub>2</sub> at appropriate times and the dorsal part of the eye was marked with an indelible marker by a stitch in the conjunctiva. Eyes were enucleated and fixed in 4% paraformaldehyde in 0.1 M phosphate-buffered saline (PBS) for 6 h, extensively washed in 0.1 M PBS, and cryoprotected by equilibration with 10% and 20% sucrose and overnight incubation in 30% sucrose. Eyes were embedded in the compound optimum cutting temperature (Tissue-Tek; Qiagen), snap frozen in liquid nitrogen/isopentane, and cryosectioned at 20 μm using a Leica CM1850 cryostat (Leica) with the eyes oriented so that the sections extended from the superior to the inferior edge. Sections were mounted on gelatin- and poly-L-lysine-coated slides and stained with bisbenzimidazole (1:10,000; Hoechst) for 1 min at room temperature to evaluate the position of the implant and retina layers. To block nonspecific binding in immunohistochemistry experiments, 0.75% horse serum for FGF2 and GFAP and 10% goat serum for IBA1 were used. Sections were incubated overnight at 4 °C with mouse monoclonal FGF2 antibody (1:200 in 0.75% horse serum; Upstate Biotechnology), rabbit polyclonal IBA1 (1:1,000 in 1% goat serum; Wako Pure Chemical Industries) and rabbit polyclonal GFAP (1:5,000 in 0.75% horse serum). Secondary antibodies, anti-rabbit IgG conjugated to Alexa Fluor 488 or Alexa Fluor 594 (Molecular Probes, Invitrogen) for IBA1 and GFAP and Alexa Fluor 488-conjugated anti-mouse IgG (Molecular Probes, Invitrogen) for FGF2, were diluted 1:200 and incubated at 37 °C for 2 h. Retinal sections were acquired by using a Nikon 80i confocal microscope. Morphometric analysis was performed on two or three animals per experimental group by imaging and analysing two slices per retina and seven fields per slice, namely: three dorsal to the implant, one in the region of the implant, and three ventral to the implant. Acquisition parameters were kept constant throughout the imaging session for comparison purposes. Mean fluorescence intensity analysis for FGF2 and GFAP was performed using the ImageJ software. Iba1 cells were manually counted in each field.

**Post-mortem characterization of implanted prostheses. Raman spectroscopy.** Raman spectra were recorded by using a commercial Renishaw In Via Raman

microscope in a back-scattering configuration, including a monochromator, notch filter system and a charge-coupled detector. Excitation wavelength: 532 nm. Samples were placed on the stage of a Leica microscope, equipped with 5×, 20×, 50× and 100× short- and long-working-distance objectives. In all measurements, laser power intensity on the sample was kept at values lower than 0.03 mW to avoid laser-induced sample degradation. All measurements were carried out at room temperature.

**Surface potential measurements.** Surface potential measurements were performed with a patch-clamp set-up (Axopatch 200B, Axon Instruments) coupled to an inverted microscope (Nikon Eclipse Ti). An LED system (Lumencor Spectra X), fibre-coupled to the fluorescence port of the microscope, provided the light for the optical excitation of the devices. The samples were illuminated with 540 nm light pulses at photoexcitation density of 222 mW mm<sup>-2</sup>. The size of the light spot is 0.23 mm<sup>2</sup>. Recordings are carried out in voltage clamp configuration by micro-manipulating freshly pulled glass pipettes (3/6 MΩ) in the close proximity (~2 μ) of the polymer/electrolyte interface. Both the pipette and the bath are filled with electrolytic Krebs–Ringers–Henseleit solution (KRH) to avoid junction potential artefacts. The measured current is set to zero under dark conditions; surface potential is then calculated by multiplying the current trace measured following illumination by the pipette resistance. All measurements were performed at room temperature. Acquisition was performed with pClamp 10 software suite (Axon Instruments) and all data were elaborated with Origin 8.0.

**Scanning electron microscopy (SEM).** SEM imaging was performed post-mortem on retinae explanted and fixed from RCS rats 6 months after implant surgery and on the relative dissected prosthesis. CO<sub>2</sub> anaesthesia and cervical dislocation were performed to euthanize the animals. The eye and retina dissection was realized under dim red light. Eyes were enucleated and transferred to carboxygenated Ames' medium (Sigma Aldrich), where the cornea, lens and part of the vitreous were removed. The tissues were then fixed in 1.25% glutaraldehyde in 0.1 mM sodium cacodylate buffer, post-fixed in 1% OsO<sub>4</sub>, 0.1 M sodium cacodylate, dehydrated, and cut into sections under a stereomicroscope. Imaging of the full and sham silk-only devices explanted from the animals and freed of tissue was also performed. The post-mortem preparations were coated with a 10 nm evaporated Au layer and observed with a JEOL-7500 electron microscope (Jeol).

**Statistical analysis.** Data are expressed as means ± s.e.m., with *n* as the number of independent animals (*n*). ANOVA followed by the Tukey's *post hoc* test was used. *p* < 0.05 was considered significant. Statistical analysis was carried out using OriginPro-8 (OriginLab Corp.) and Prism (GraphPad Software).

**Data availability.** The experimental data that support the figures within this paper and other findings of this study are hosted at the Istituto Italiano di Tecnologia and can be accessed by contacting the corresponding author.

## References

51. Stavrinidou, E. *et al.* Direct measurement of ion mobility in a conducting polymer. *Adv. Mater.* **25**, 4488–4493 (2013).
52. Pizzorusso, T. *et al.* Structural and functional recovery from early monocular deprivation in adult rats. *Proc. Natl Acad. Sci. USA* **103**, 8517–8522 (2006).
53. Huang, Z. J. *et al.* BDNF regulates the maturation of inhibition and the critical period of plasticity in mouse visual cortex. *Cell* **98**, 739–755 (1999).
54. Marini, C. *et al.* Direct inhibition of hexokinase activity by metformin at least partially impairs glucose metabolism and tumor growth in experimental breast cancer. *Cell Cycle* **12**, 3490–3499 (2013).